Application of Wavefield Continuation to the Inversion of Refraction Data

George A. McMechan

Robert W. Clayton

Walter D. Mooney

Abstract

Three examples of the inversion of refraction data by downward continuation illustrate the applicability of the method to field data. The first example is a refraction profile from the Mojave Desert, California. These data are spatially aliased and contain clear evidence of lateral inhomogeneity. The inversion in this case produces a broken image in the slowness-depth domain due to the lateral inhomogeneity, but a useful average velocity model is still obtained. The second example is a shallow marine reflection profile. Here, the truncation effects due to the finite horizontal aperture of the recording cable produce artifacts in the slowness-depth domain. The velocity model is, however distinct from these artifacts, and the presence of strong pre-critical reflections aids in the inversion. The third example is another shallow marine reflection profile. The inversion of these data illustrate the utilization of constraints provided by multiples as well as primary arrivals.

Introduction

Recently, a downward continuation method was presented for the inversion of densely recorded refraction data (Clayton and McMechan; 1981a,b). This technique transforms the entire recorded data wavefield from the time-distance $(t-x)$ domain into the slowness-depth $(p-z)$ domain. The resulting velocity-depth locus is a focussed image in the $p-z$ domain, and the uncertainty in the solution is indicated by the width and coherence of this

image. There are two basic assumptions in the procedure which limit its general applicability. The first is the assumption of lateral homogenity of the velocity structure, and the second is the assumption that the data are sufficiently well sampled in the spatial dimension that they can be treated as a wavefield.

In this paper we present three examples of the application of this method to real refraction data. The main object of the paper is to illustrate the technique when applied to data which do not rigidly satisfy the assumptions mentioned above. Before considering the data, a brief review of the inversion procedure is given.

The downward continuation method consists of two linear, reversible wavefield transformations (Clayton and McMechan, 1981a). The first transformation is a slant stack of the $t-x$ data (Schultz and Claerbout, 1978; Chapman, 1978; McMechan and Ottolini, 1980; Chapman, 1981)

$$S(\tau,p) = \int_{-\infty}^{+\infty} P(\tau+px,x)dx \tag{1}$$

Here $P(t,x)$ is the observed (seismogram) wavefield, $S(\tau,p)$ is the transformed wavefield, p is the horizontal slowness, τ is the time intercept, x is the shot-receiver distance, and t $(=\tau+px)$ is the traveltime. The slant stack integral (1) produces a wavefield in which the $p-\tau$ curve (the curve of Bessonova *et al.*, 1974) is imaged. This step is done only once. The slant stack itself may be viewed as a mathematical transformation which makes no physical assumptions about the nature of the field. However, to interpret p as the horizontal slowness, it is necessary to assume lateral homogeneity. Also, to produce a reasonable tau curve image, it is necessary that the data not be severely aliased (Brocher and Phinney, 1981).

The second transformation is an iterative downward continuation of $S(\tau,p)$:

$$s(p,z) \equiv S(\tau=0,p,z) = \int S(\omega,p,z=0)e^{-i\omega\Psi(p,z)}\,d\omega \tag{2}$$

where

$$\Psi(p,z) = 2\int_0^z |v^{-2}(z)-p^2|^{1/2}\,dz$$

In equation (2), $s(p,z)$ is the solution wavefield, $v(z)$ is velocity as a function of depth z, and ω is the temporal frequency. Implicit in equation (2) is the assumption of lateral homogenity of the velocity model because the up and downgoing raypaths are assumed to be identical. This transformation of $S(\tau,p)$ is repeated with successive modifications to $v(z)$ until the downward continued wavefield $s(p,z)$ images the input $v(z)$ function. This

condition of stationarity indicates that convergence has been achieved [i.e., the $v(z)$ function that produces stationarity is the solution]. A more detailed discussion is given by Clayton and McMechan (1981a).

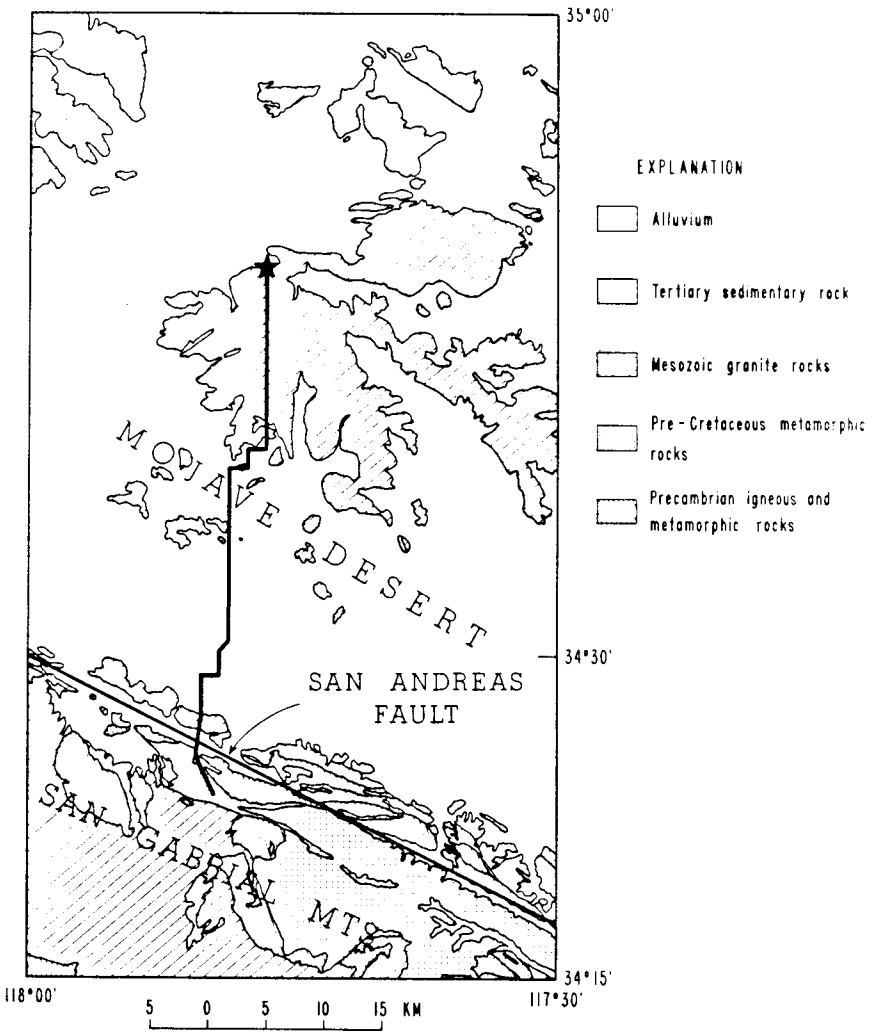

FIG. 1. Location of the Mojave Desert refraction profile. The star is the shot point. The recording instruments were placed along the line extending southward from the shot point. The seismograms recorded on this profile are shown in Figure 2.

The main restrictions on the applicability of the downward continuation approach to inversion are that typical refraction data are spatially aliased, and that the Earth structure is often laterally inhomogeneous. In the sections that follow, realistic examples are considered that do not rigidly satisfy the assumptions of the method, and hence serve to illustrate the robustness and utility of the wavefield approach even when the data are not ideal. Three data sets are presented. The first profile is composed of vertical component velocity

records from the Mojave Desert, and the other two are suites of acoustic responses recorded by hydrophone cables in shallow marine environments.

The Mojave Desert Profile

In the fall of 1980, the United States Geological Survey (USGS) conducted an extensive refraction project in the Mojave Desert of southern California. Only a portion of these data will be analyzed here. The location of the profile we have chosen is shown in Figure 1, and the data traces are shown in Figure 2.

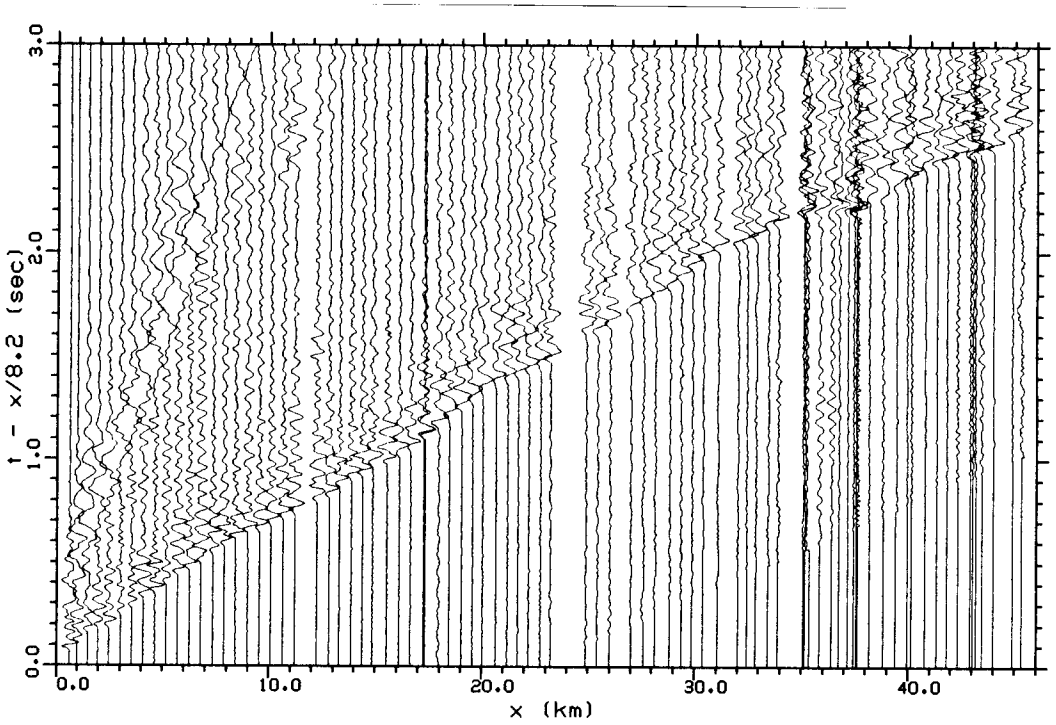

FIG. 2. Record section from the Mojave Desert data with a reduction velocity of 8.2 km/s. This profile is a composite of recordings of two shots, a smaller one recorded at $x < 10$ km and a larger one recorded at $x > 10$ km. The records are normalized so each has the same maximum amplitude.

A number of features are evident in the data (Figure 2). The first arrivals do not form a smooth locus of constantly decreasing slope (p), as would be observed if the Earth structure were laterally homogeneous. Most of these fluctuations can be attributed to surficial sediments (Fuis, 1981). Others, such as the early arrivals near x=37 km, are apparently

related to changes of structure at faults (see Figure 1). These traveltime fluctuations do not prevent analysis of the data by wavefield transformation but as discussed below they do contribute significantly to the uncertainty associated with the best fit laterally homogeneous model.

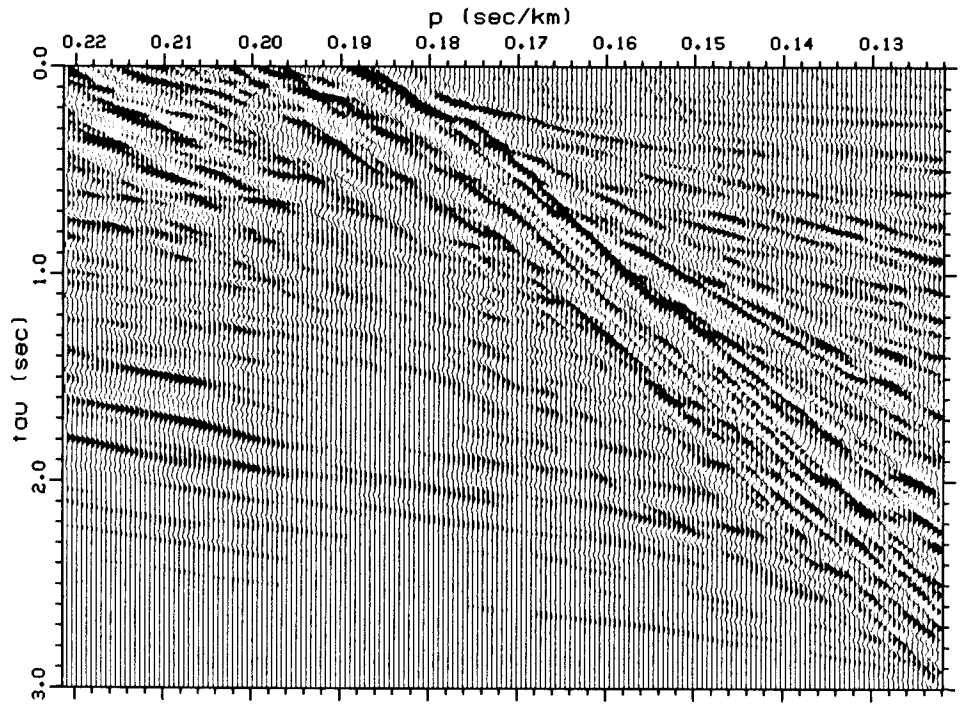

FIG. 3. Slant stack ($p-\tau$) wavefield obtained by transformation of the Mojave Desert data in Figure 2 via equation (1). Iterative downward continuation of this wavefield produces the velocity-depth model.

Figure 3 shows the slant stack of the data in Figure 2. As the data traces are unequally spaced, a weighing that depends on trace separation was employed in slant stacking (cf. Henry *et al.*, 1981). A fairly coherent image can be seen traversing this wavefield in the (p,τ)-region from (0.188, 0.0) to (0.138, 1.6). The image does have some "en echelon" branches beside the main locus and some regions where τ is not monotonically decreasing that are due to the fluctuations in arrival times mentioned above. These anomalies are easier to see in Figure 4.

Iterative downward continuation of the $p-\tau$ wavefield in Figure 3 produces the slowness-depth image displayed in Figure 4. The solid line in Figure 4 is the velocity

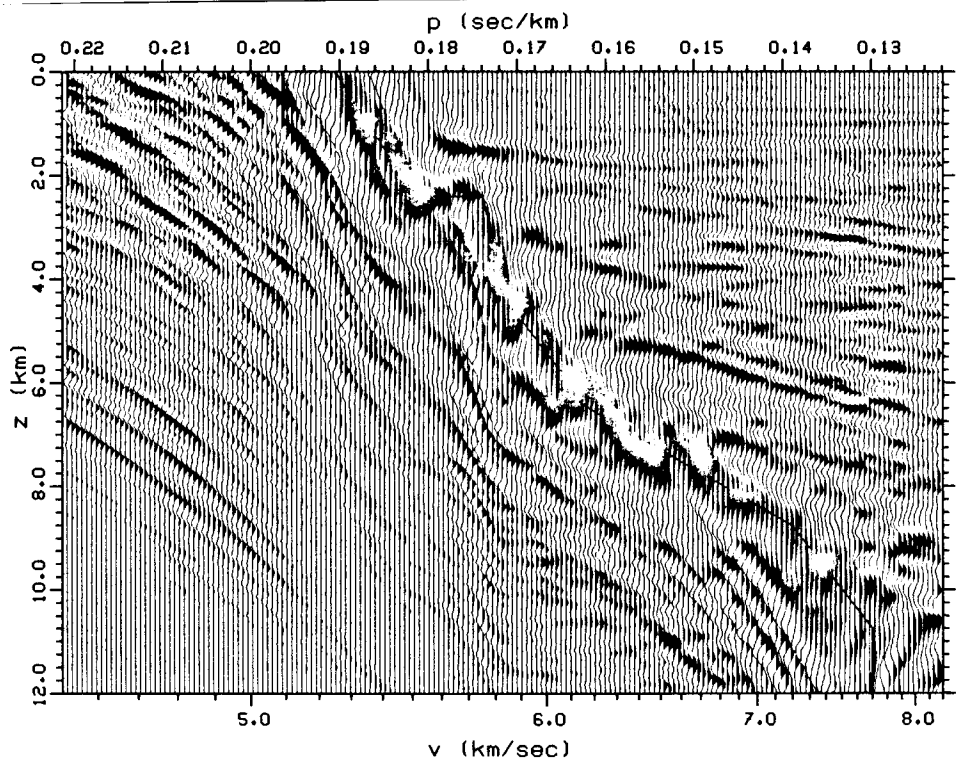

FIG 4. The slowness-depth $(p-z)$ wavefield of the Mojave Desert data at convergence. The solid line superposed on the wavefield is the velocity-depth model used in the final iteration in the downward continuation. The coincidence of the solid line and the image shows the convergence.

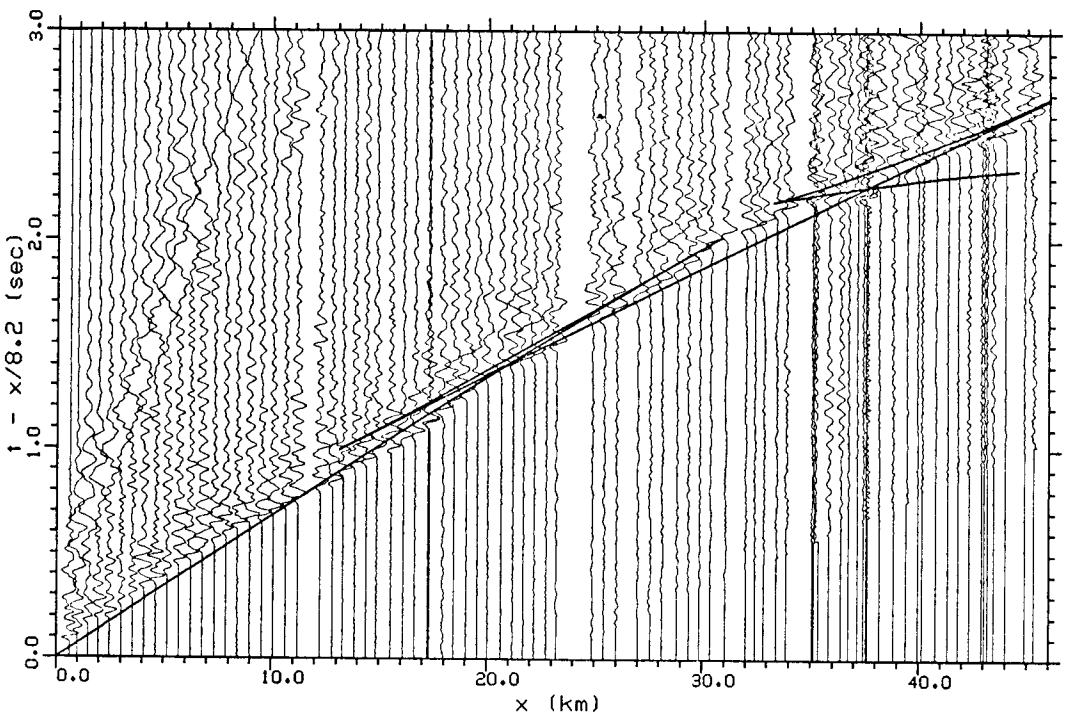

FIG. 5. Comparison of observed traveltimes with those computed for the velocity depth function shown as the solid line in Figure 4.

function at the final iteration and it coincides with the dominant image in the downward continued $p-z$ wavefield. However, because of the lateral variations in structure along the profile, the image is broken and sometimes multivalued. The convergence condition, as defined by the solid, monotonic velocity-depth curve can therefore be considered only as an average laterally homogeneous approximation to the velocity structure along the profile. The uncertainty in this representation of the structure, which is indicated by the width and incoherence of the image, is ± 0.8 km depth. This uncertainty in depth can be attributed to a composite of two effects. First, the time resolution and frequency content in the original data is seen in the width of the individual branches of the split image, which accounts for about half the variation. The multiplicity of branches due to lateral velocity changes accounts for the remainder.

As a check on the adequacy of the model obtained, traveltimes were computed for the model by ray tracing. (Note that, up to this point, traveltimes have not been directly used to constrain the model). The resulting traveltime curve is superimposed on the data in Figure 5. In general, the model produces a smooth curve that fits the first arrival observations to within 0.05 seconds. The fit is early at some distances and late at others, indicating that we have indeed obtained a reasonable average velocity function by downward continuation.

Two triplications are evident in the traveltime curve in Figure 5. The one that occurs at 13 km $< x <$ 31 km is due to the rapid velocity increase near 2.3 km depth (Figure 4). This triplication may be real as there appears to be an increase in waveform complexity near the first arrivals over this distance range, which is consistent with the existence of a triplication. On the other hand, this feature may be an artifact introduced by fortuitous correlations across the variations in first arrival times due to lateral structure changes in this region. The latter interpretation is supported by the absence of the expected pre-critical reflection image in Figure 4. The pre-critical reflection would lie horizontal and touch the main image at the depth of the reflector (2.3 km). Examples of pre-critical reflections are shown in Figure 11 below.

The second triplication lies at $x >$ 33 km in Figure 5. This feature is clearly due to lateral rather than vertical velocity variations, as the highest velocity branch results from coherence of energy strongly affected by the San Andreas Fault (near x = 37 km). Consequently, the velocities in the model in Figure 4 are not reliable below 6 km depth.

In order to further investigate the stability of the solution in Figure 4, the model was altered to decrease the velocity gradient near 2.3 km depth. This model is shown as the solid line superimposed on the wavefield obtained by downward continuation with it in Figure 6. This model does not give the wavefield stationarity required for convergence (note the shift of the wavefield in Figure 6 relative to that in Figure 4); however, as is shown in Figure

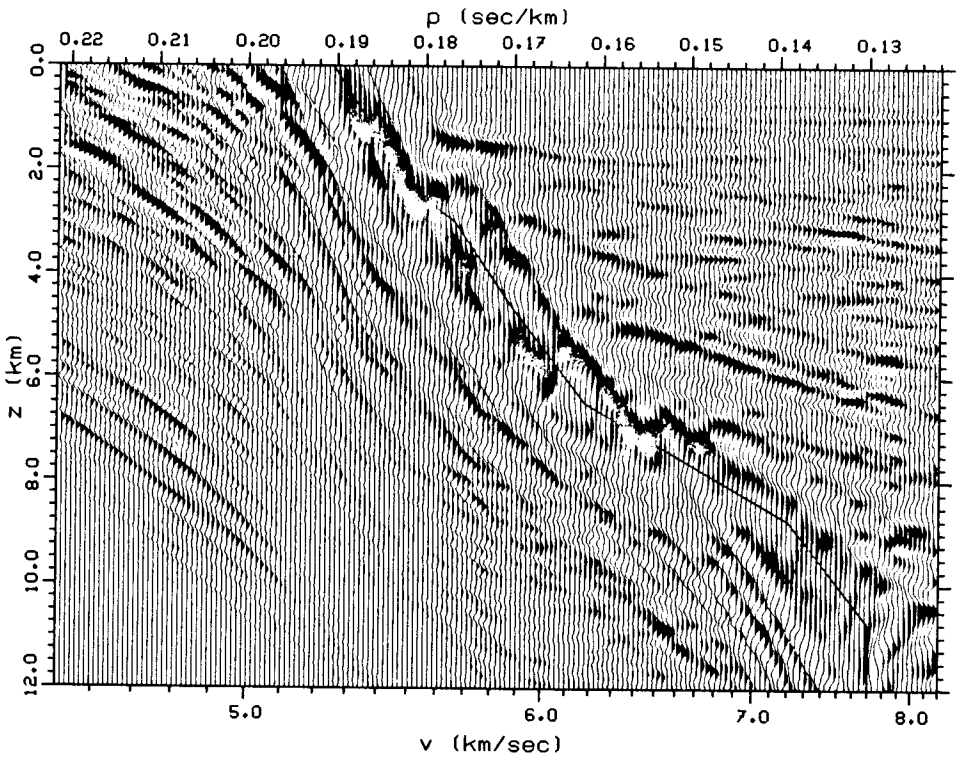

FIG 6. An acceptable, but unconverged downward continuation solution. The solid line is a velocity-depth curve that produces acceptable traveltimes (see Figure 7) but does not correspond to stationarity of the $p-z$ wavefield.

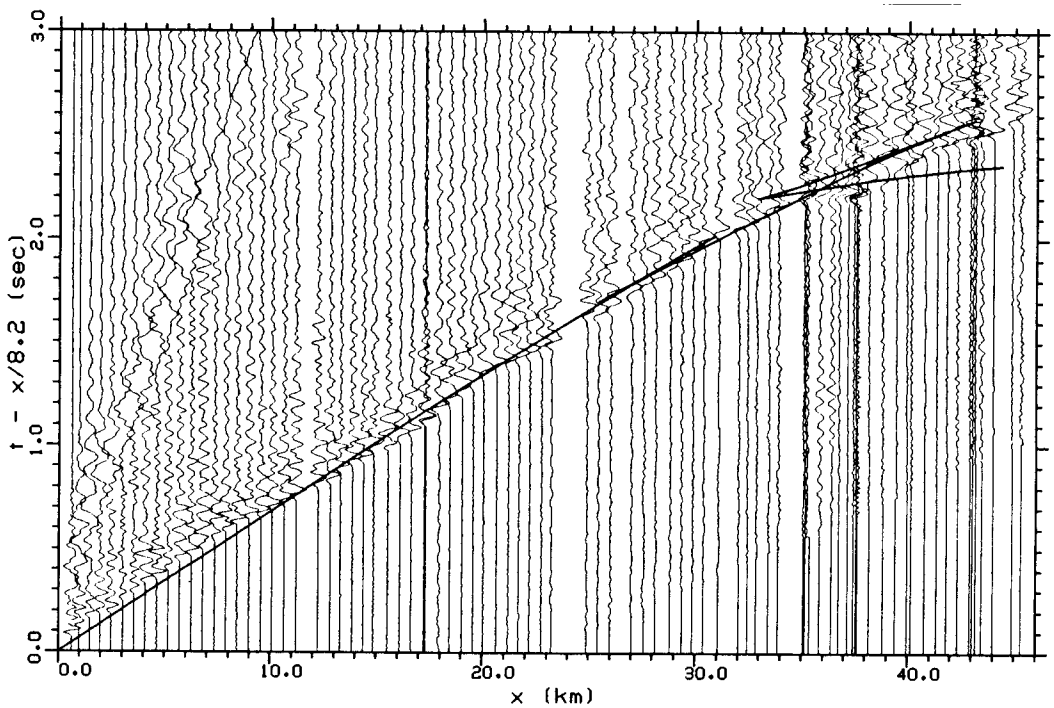

FIG. 7. Comparison of observed traveltimes with those computed for the unconverged model in Figure 6. The calculated traveltimes are shown as the solid line.

7, it fits the observed traveltimes as well as the convergent model does. To choose between the two models is difficult. The first model has converged, but this is a valid indication of a correct solution primarily for laterally homogeneous media. The second model fits the observed times adequately and is slightly simpler, but has not converged. For comparison, Figure 8 shows the two average models discussed here along with a shaded area that corresponds to the estimated range of velocities as determined for the same region by two-dimensional ray tracing (Fuis, 1981). The velocity in the uppermost 2.5 km, which corresponds to fractured granite, is most variable; at these depths our models generally lie within the shaded region. Below 2.5 km the position and velocity gradient of our converged model (curve 1) correspond closely to those of Fuis; those of the smoothed model (curve 2) do not.

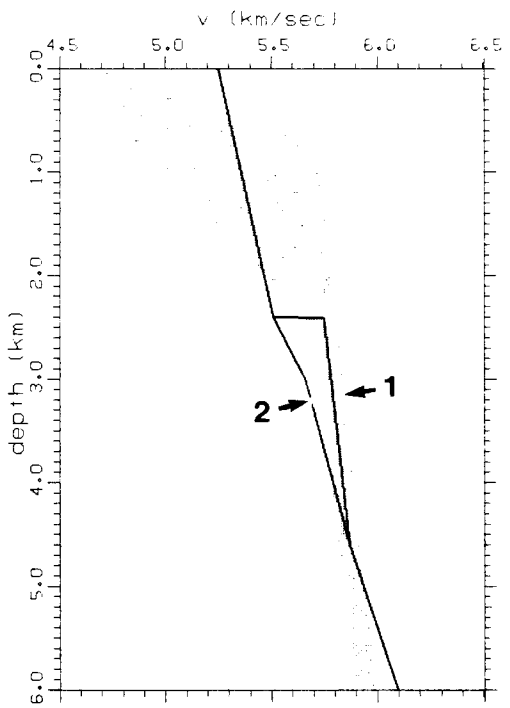

FIG. 8. Comparison of velocity profiles for the Mojave Desert. Model 1 is that in Figure 4, Model 2 is that in Figure 6, and the shaded area is an estimate of the range of velocities in this area as obtained independently by two-dimensional ray tracing by Fuis (1981).

In summary, this analysis of the Mojave Desert data illustrates some of the trade-offs that occur when structure varies laterally. Specifically, a reasonable, average velocity-depth curve can be stably estimated, but the finer details of the curve may be related to lateral rather than vertical velocity variations. These effects are not confined to wavefield analysis, but the wavefield approach has the advantage of being relatively unbiased as the significance of any region of coherent energy in the data is not established until convergence is obtained. The identification of the possible triplication near 20 km is an example of this.

A Shallow Marine Profile Containing Pre-critical Reflections

In a laterally homogeneous region, data in both the common-shot recording geometry and the common midpoint interpretation coordinates used in seismic exploration can be directly inverted by wavefield transformation. In this section we present an example of the analysis of a common midpoint gather containing the acoustic response of the uppermost 1 km of sediments in a shallow marine environment. The data are shown in Figure 9.

Figure 10 shows the slant stack of the data in Figure 9. There are some artifacts visible in this wavefield; the most prominent ones (labeled T in Figure 10) are due to the truncation of the data at the two ends of the recording cable and appear as coherent straight lines. The $p-\tau$ image of interest consists of two types of curves. The first is the main trajectory that lies in the (p,τ)-region from (0.69, 0.0) to (0.45, 0.6). The second type corresponds to pre-critical reflections which appear as hyperbolic trajectories in the upper right part of Figure 10 (e.g. those labeled A, B and C).

The strong pre-critical reflections in these marine data are useful constraints in the downward continuation of the $p-\tau$ wavefield to produce the model (the solid line in Figure 11). When the correct velocity function is used, pre-critical reflections produce a straight, horizontal image in the $p-z$ plane at the depth of the reflector. The image is horizontal because all the p values associated with the reflection event bottom at the same depth. The uppermost reflection (A) in Figure 11 is from the water-sediment interface. The image is poorly defined between (A) and the inter-sediment reflection (B). The RMS velocity is, however, apparently correct because image (B) is straight and horizontal. Similarly, image (C) corresponds to a reflector at about 0.3 km depth. A major reason that those parts of the image lying between reflections are not well defined is that the cable length is not sufficient to contain all the refracted and post-critical reflection energy. The clearest part of the image is from 0.5 to 1.0 km depth where there is a coherent trajectory indicating a nearly linear increase of velocity with depth. Such an increase is consistent with the observation

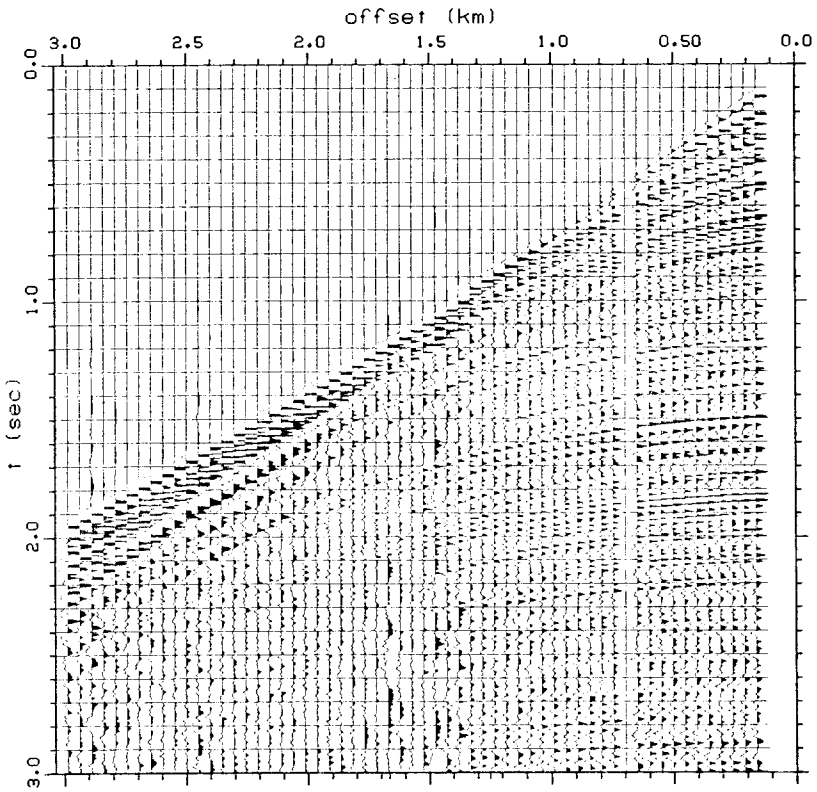

FIG. 9. Common midpoint marine profile. These data are plotted in the reflection seismology convention of time increasing downward (in contrast to the refraction format used for Figure 2). Since this is a common midpoint gather, offset rather than shot distance has been plotted. This example contains prominent pre-critical reflections that are used as constraints for velocity inversion.

of a gently curved first arrival branch in the traveltime curve between the 1.5 and 3.0 km offsets in Figure 9. The depth resolution, as defined by the width of the image at convergence, varies from about ± 0.03 km near the surface to about ± 0.07 km near 1.0 km depth.

As a check of the model in Figure 11, the traveltimes corresponding to this model were computed and superimposed on the data as shown in Figure 12. In addition to the reflections from the three velocity steps mentioned above, reflection times from the high velocity gradient near 0.45 km-depth (labeled D) is also shown. All four reflections appear to be expressed in the data, particularly at the near offsets. Evidence for additional small velocity steps is seen in the traveltime and $p-z$ domains. We have attempted to image only the major ones.

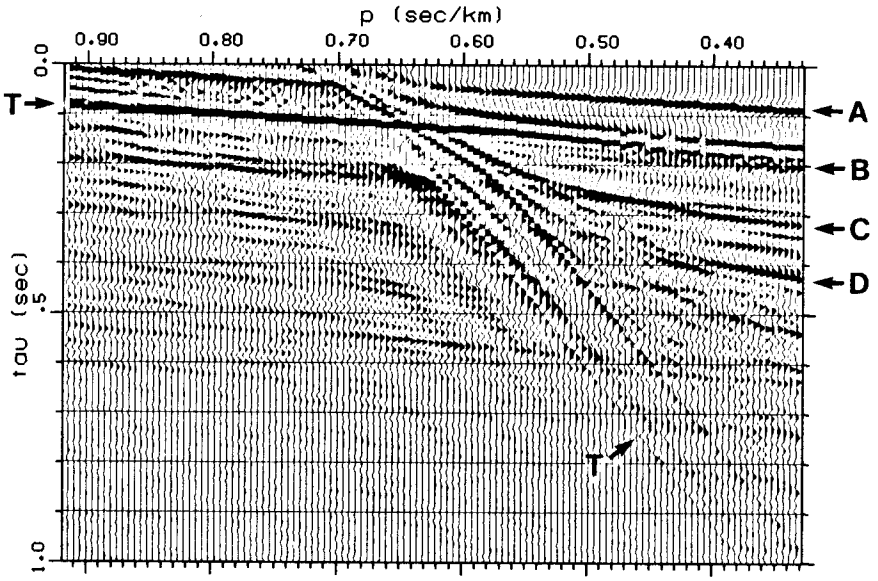

FIG. 10. Slant stack ($p-\tau$) wavefield obtained by transformation of the marine data in Figure 9. Iterative downward continuation of this $p-\tau$ wavefield converges with the velocity profile and $p-z$ wavefield in Figure 11. The curves labeled A through D are pre-critical reflections. The curves labeled T are cable truncation artifacts.

Figure 13 contains the superposition of our velocity profile (converted from depth to two-way traveltime) upon a near offset reflection data section. The inversion of the refractions by wavefield transformation produced a model whose two-way traveltimes to the main reflectors that are compatible with those observed in the near-offset section. Velocity increases correspond to the main reflection arrivals in the data.

A Shallow Marine Profile Containing Water Multiples

Marine data recorded over a hard bottom typically contain prominent multiple reflections whose peglegs are confined to the water column. (Note that these multiples are not the same as the PP-type refracted multiples analyzed by Clayton and McMechan (1981b)). Analysis of such data can be accomplished by imaging the multiples concurrently with the primary energy. The purpose of the following example is to demonstrate concurrent inversion. The acoustic data that are shown in Figure 14 contain at least four water multiples, of which the first two are directly included in the wavefield inversion presented below. The result of this inversion consists of three images of the velocity-depth profile down to 0.6 km depth.

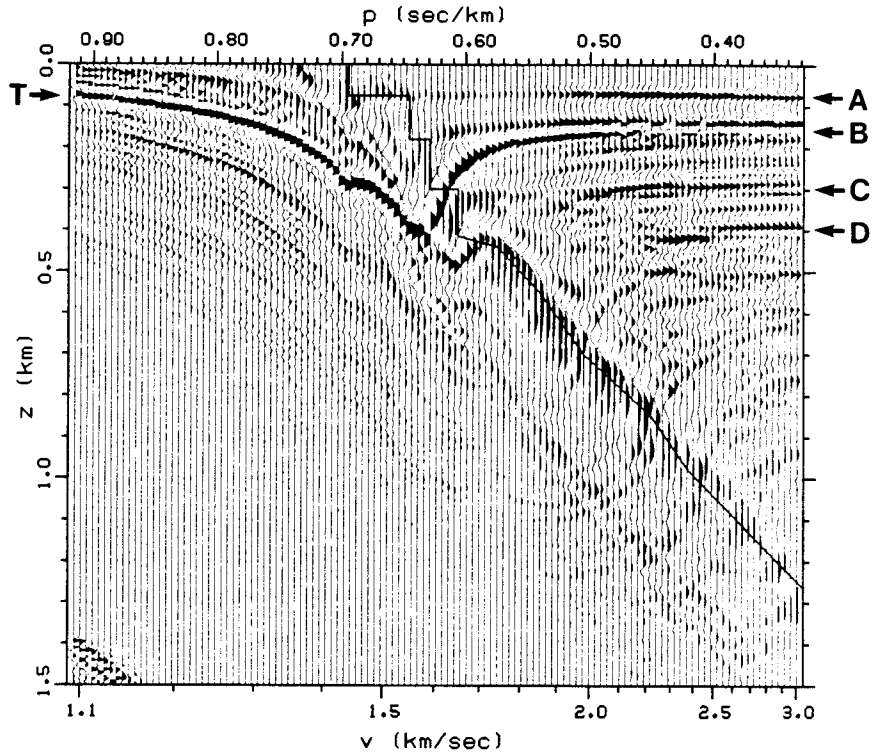

FIG. 11. The $p-z$ wavefield of the marine data profile of Figure 9 at convergence. The solid line superimposed on the wavefield is the velocity-depth function used in the downward continuation. Labeled branches correspond to those labeled in Figures 10, 12 and 13.

Figure 15 shows the slant stack of the data in Figure 14. In this wavefield a number of water multiples (labeled M) are visible. The precise location of the primary $p-\tau$ locus is not as clear as in the previous examples because of interference between the primaries and multiples, but it is located approximately between (p,τ) from (0.67, 0.0) to (0.40, 0.5).

In order to identify and image the multiples, three $p-\tau$ wavefields were concurrently downward continued into $p-z$ space. The first of these is the complete $p-\tau$ wavefield shown in Figure 15. The second is a new $p-\tau$ wavefield $(p-\tau')$ constructed from the first by shifting each p trace toward smaller τ. The amount of shift at each p is equal to the τ of the primary water bottom reflection of the same p:

$$\tau'(p) = \tau(p) - 2\frac{h}{v}\left(1 - p^2v^2\right)^{1/2} \tag{3}$$

where h and v are the thickness and velocity of the water layer. Inversion of this modified wavefield images the first multiple. Similarly, for imaging the second multiple, another $p-\tau$ wavefield was constructed by subtracting twice the primary water reflection τ at each p. The result of concurrent imaging of these three $p-\tau$ wavefields is the three $p-z$

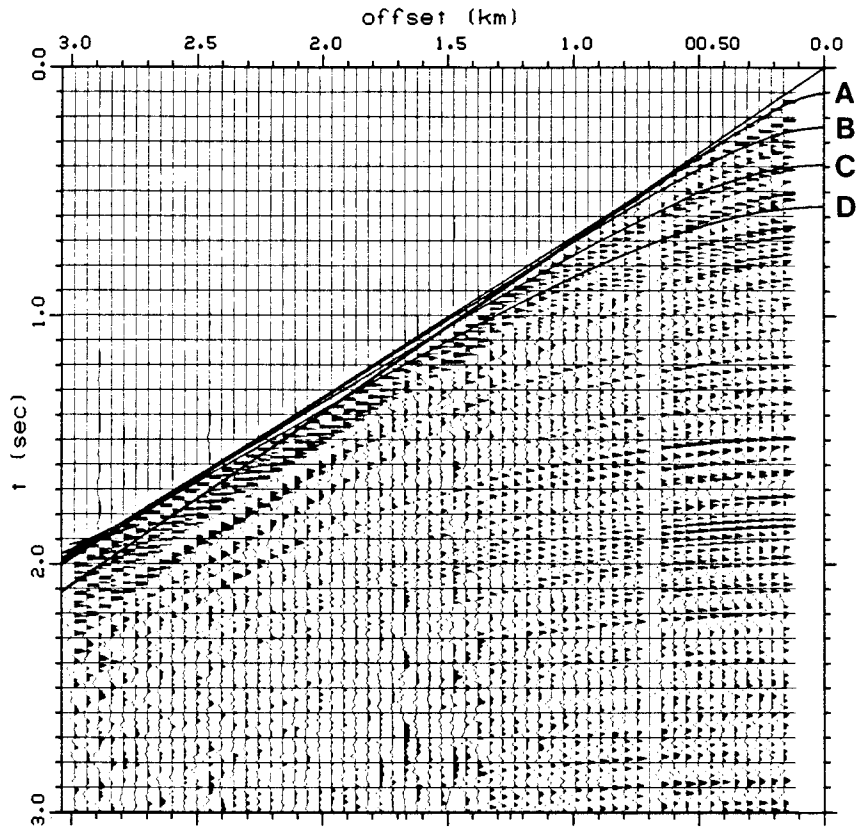

FIG. 12. Comparison of observed and calculated traveltimes. The solid lines superposed on the data are times predicted from the model in Figure 11. Arrivals are labeled to correspond to those in Figures 10, 11 and 13.

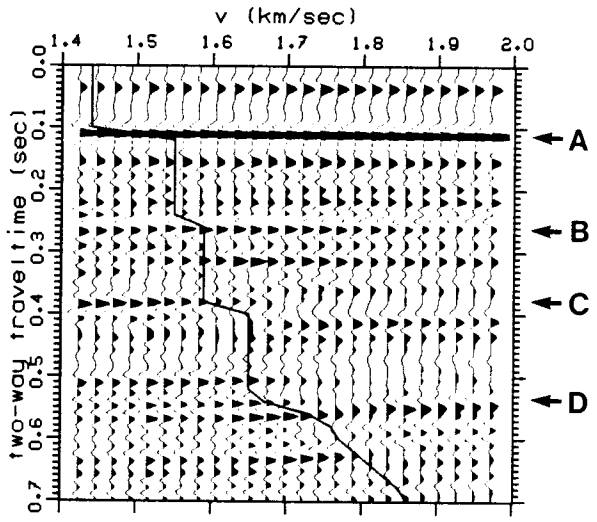

FIG. 13. Overlay of velocity model on data section. The solid curve is the two-way traveltime equivalent of the velocity-depth function in Figure 11. The wavefield upon which it is plotted is a near offset reflection section. The first (left) trace is the near offset trace from the common midpoint data used to derive the velocity profile. The reflections are labeled to correspond to those in Figures 10 to 12.

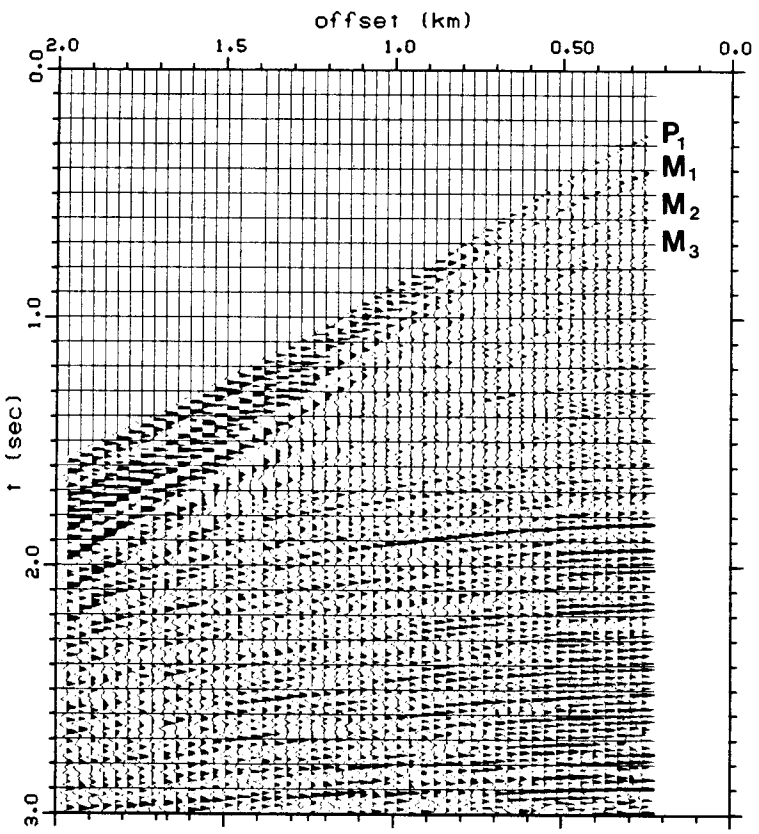

FIG. 14. Common midpoint marine profile. These data contain free-surface water multiples that are used as constraints in velocity inversion. P_1 is the primary water bottom reflection, M_1 is its first multiple, M_2 is its second, and so forth.

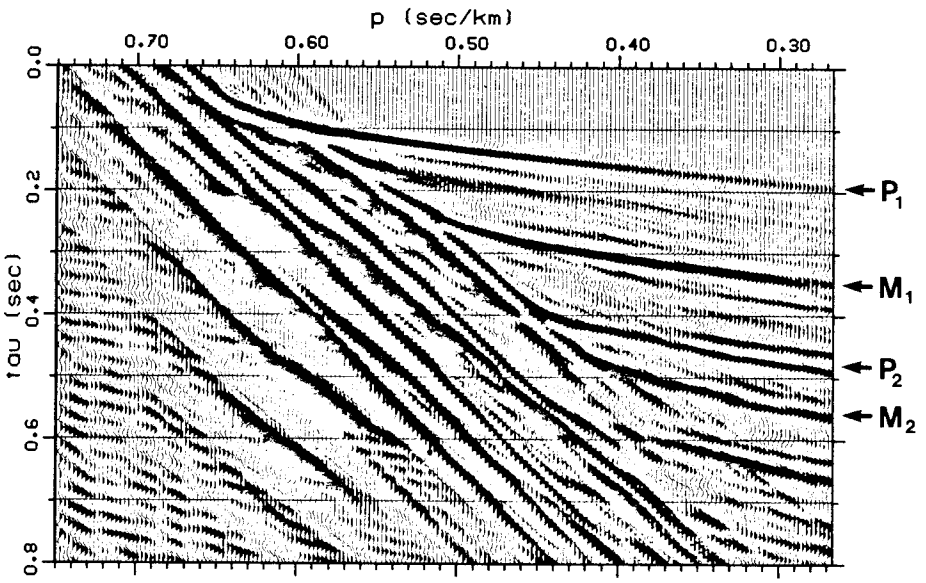

FIG. 15. Slant stack ($p-\tau$) wavefield obtained by transformation of the marine data in Figure 14. In this wavefield a number of water column multiples are present. P_1 is the primary water bottom reflection, M_1 is its first multiple, M_2 is its second, and so forth. P_2 is another primary reflection. The imaging of these data produce the $p-z$ wavefields in Figure 16.

wavefields in Figure 16. The solid line superimposed on all three $p-z$ wavefields corresponds to the final $p-z$ locus. The uncertainty in this locus is seen to be of the order of $\pm$ 0.025 km. In Figure 16a, P_1 is the pre-critical primary water-bottom reflection and P_2 is the pre-critical primary reflection from a discontinuity near 0.35 km depth. Both of these appear horizontal in the $p-z$ wavefield (a). The non-horizontal loci M_1 and M_2 are the first two water column multiple reflections. In (b), where the $p-\tau$ wavefield was shifted by τ corresponding to one water reflection, the primary energy (1) lies above the $p-z$ locus (2). In (c) where the shift is double, two images (1 and 2) lie above the $p-z$ locus (3).

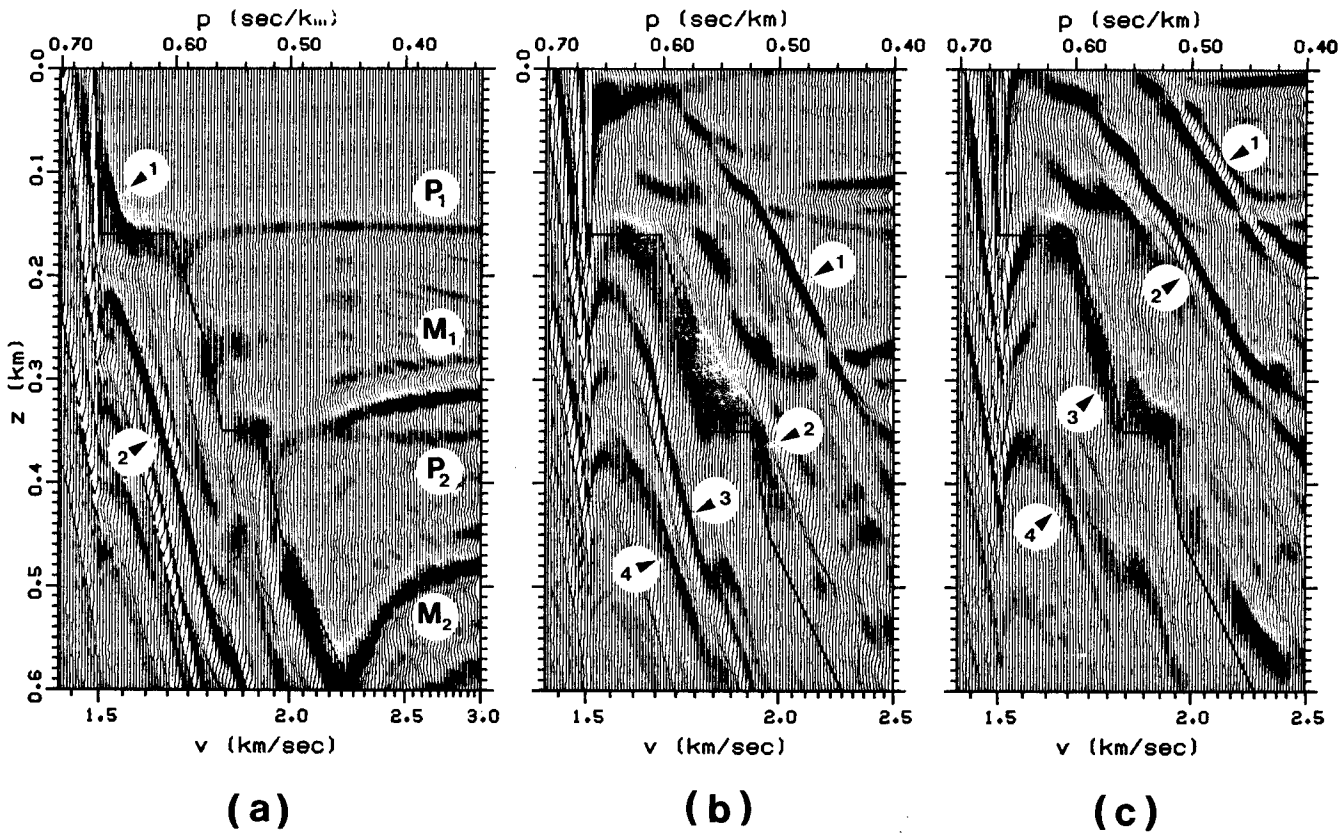

FIG. 16. Concurrent imaging of three $p-z$ wavefields. The left (a) panel is the inversion based on the primary energy; the center (b) panel is for the first multiple; the right panel (c) is for the second multiple. All three image the same $p-z$ curve (the solid line that is superimposed on each). In each panel, the successive images are numbered: 1 for the primary image, 2 for the first multiple image, 3 for the second multiple, and so forth. Branches labeled M and P are pre-critical reflections discussed in the text.

This example illustrates the interpretation problem associated with water multiples. Specifically, pre-critical multiple reflections cut across the primary branches. This interference produces an incoherent primary image. When multiples are concurrently inverted with the primary energy however, a coherent picture emerges as successive multiple loci fill in the ambiguous portions. Figure 17 contains a comparison of our results with those of Schultz (1981) who independently analyzed this same data set by a layer stripping method. Again, the results are compatible with each other.

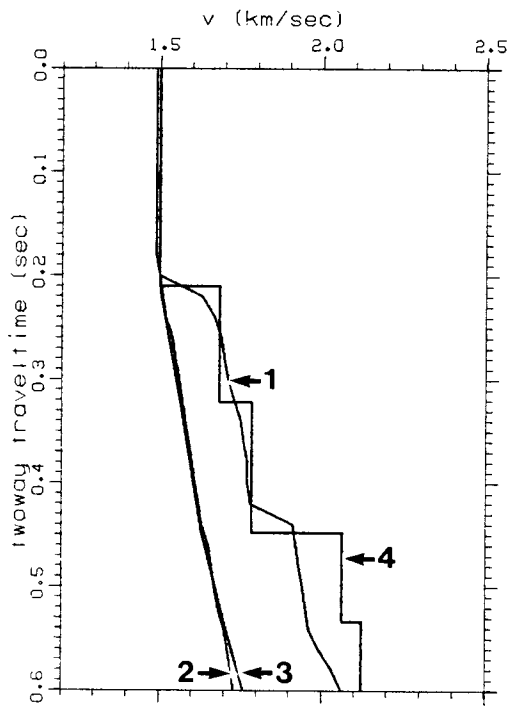

FIG. 17. Comparison of two velocity analyses of the data in Figure 14. Curve 1 is the two-way traveltime profile corresponding to the velocity profile plotted in the three panels of Figure 16); 2 is the corresponding RMS time profile; 3 is the RMS time profile of Schultz (1981); 4 is the time profile computed from 3. Curve 1 is to be compared with 4; 2 with 3.

Discussion and Summary

One of the advantages of the wavefield transformation approach is that no preprocessing of the data is required. The complete data set is used in raw form, so the final image contains no arbitrary selection of data. For analysis of large scale refraction profiles, such as the Mojave Desert data, wavefield transformation produces a solution in a matter of hours. For exploration (reflection) oriented processing, wavefield transformation of

refractions provides a method of extracting independent velocity information from a portion of the wavefield that has previously been neglected by conventional analyses.

The method of refraction inversion by wavefield transformation has been illustrated by application to three rather different data sets, one recorded on land in a common-shot refraction geometry, and the other two recorded in shallow marine environments with standard acoustic exploration cables. In all three cases, the results obtained are compatible with those of conventional processing. Wavefield transformation is seen to be robust, unbiased, and particularly suited to processing large volumes of data. These features, combined with the conceptual elegance involved in forming the solution from the data itself, encourage further development and application of the method.

Acknowledgements

We thank the United States Geological Survey for providing the Mojave Desert data, CONOCO for providing the first marine data set, and Digicon for the second.

REFERENCES

Bessonova, E.N., Fishman, V.M., Ryaboyi, V.Z., and Sitnikova, G.A., 1974, The Tau method for inversion of travel times -I. Deep seismic sounding data: *Geophys. J.*, v. 36, p. 377-398.

Brocher T.M., and Phinney R.A., 1981, Inversion of slant stacks using finite-length record sections, submitted to *J. Geophys. Res.*

Chapman, C.H., 1978. A new method for computing synthetic seismograms, *Geophys. J. R. astr. Soc.*, 54, 481-518.

Chapman, C.H., 1981. Generalized Radon transform and slant stacks, *Geophys. J. R. astr. Soc.*, submitted.

Clayton, R.W., and McMechan G.A., 1981a. Inversion of refraction data by wavefield continuation, *Geophysics*, in press.

Clayton, R.W., and McMechan G.A., 1981b. Inversion of refracted free-surface multiples by wavefield continuation, submitted to *Geophys. J. R. astr. Soc.*

Fuis, G.S., 1981, Crustal structure of the Mojave Desert. U. S. Geol. Surv. Open File Report 1981-???.

Henry, M., Orcutt, J.A., and Parker, R.L., 1980. A new method for slant stacking refraction data, *G. R. L.*, 7, 1073-1076.

McMechan, G.A., and Ottolini, R., 1980. Direct observation of a p-τ curve in a slant stacked wavefield, *Bull. Seism. Soc. Am.*, 70, 775-789.

Schultz, P.S., 1981. A method for direct estimation of interval velocities in the near surface, preprint.

Schultz, P.S., and Claerbout, J.F., 1978. Velocity estimation and downward continuation by wave front synthesis, *Geophysics*, 43, 691-714.

Hofstadter's Law:
It always takes longer than you expect, even when you take Hofstadter's Law into account.

Surprise your boss. Get to work on time.

Hurewitz's Memory Principle:
The chance of forgetting something is directly proportional to.....to.....uh.....

Message will arrive in the mail. Destroy, before the FBI sees it.

Bank error in your favor. Collect $200.

Give thought to your reputation. Consider changing name and moving to a new town.

The brain is a wonderful organ; it starts working the moment you get up in the morning, and does not stop until you get to school.

Tonights the night: Sleep in a eucalyptus trees.

You will be a winner today. Pick a fight with a four-year-old.

Lubarsky's Law of Cybernetic Entomology:
There's always one more bug.

The seven eyes of Ningauble the Wizard floated back to his hood as he reported to Fafhrd: "I have seen much, yet cannot explain all. The Gray Mouser is exactly twenty-five feet below the deepest cellar in the palace of Gilpkerio Kistomerces. Even though twenty-four parts in twenty-five of him are dead, he is alive.

Now about Lankhmar. She's been invaded, her walls breached everywhere and desperate fighting is going on in the streets, by a fierce host which out-numbers Lankhamar's inhabitants by fifty to one -- and equipped with all modern weapons. Yet you can save the city."

"How?" demanded Fafhrd.

Ningauble shrugged. "You're a hero. You should know."